PROCEEDINGS A

rspa.royalsocietypublishing.org

Research

Cite this article: DeVoria AC, Mohseni K. 2017 A vortex model for forces and moments on low-aspect-ratio wings in side-slip with experimental validation. *Proc. R. Soc. A* **473**: 20160760.
http://dx.doi.org/10.1098/rspa.2016.0760

Received: 7 October 2016
Accepted: 27 January 2017

Subject Areas:
fluid mechanics

Keywords:
low-aspect-ratio wings, roll stall, high angle of attack

Author for correspondence:
Kamran Mohseni
e-mail: mohseni@ufl.edu

A vortex model for forces and moments on low-aspect-ratio wings in side-slip with experimental validation

Adam C. DeVoria[1] and Kamran Mohseni[1,2]

[1]Department of Mechanical and Aerospace Engineering, and
[2]Department of Electrical and Computer Engineering,
University of Florida, Gainesville, FL 32611, USA

KM, 0000-0002-1382-221X

This paper studies low-aspect-ratio ($\mathcal{AR}$) rectangular wings at high incidence and in side-slip. The main objective is to incorporate the effects of high angle of attack and side-slip into a simplified vortex model for the forces and moments. Experiments are also performed and are used to validate assumptions made in the model. The model asymptotes to the potential flow result of classical aerodynamics for an infinite aspect ratio. The $\mathcal{AR} \to 0$ limit of a rectangular wing is considered with slender body theory, where the side-edge vortices merge into a vortex doublet. Hence, the velocity fields transition from being dominated by a spanwise vorticity monopole ($\mathcal{AR} \gg 1$) to a streamwise vorticity dipole ($\mathcal{AR} \sim 1$). We theoretically derive a spanwise loading distribution that is parabolic instead of elliptic, and this physically represents the additional circulation around the wing that is associated with reattached flow. This is a fundamental feature of wings with a broad-facing leading edge. The experimental measurements of the spanwise circulation closely approximate a parabolic distribution. The vortex model yields very agreeable comparison with direct measurement of the lift and drag, and the roll moment prediction is acceptable for $\mathcal{AR} \leq 1$ prior to the roll stall angle and up to side-slip angles of 20°.

1. Introduction

The recent interest in the applications of microaerial vehicles (MAVs) has led to a great deal of research in several related areas, such as aerodynamic loading [1], flight control [2–4] and vehicle design [5]. Classical

THE ROYAL SOCIETY PUBLISHING

aerodynamic techniques and analyses are typically inapplicable to the low-Reynolds-number flight regime in which most MAVs operate (5×10^4–1×10^5), which has impeded a thorough understanding of the resulting aerodynamics. This is largely due to the fact that the flow field is inherently three-dimensional and often times unsteady, as well as being dominated by flow separation and viscous effects. Furthermore, most MAVs consist of a lifting surface of low aspect ratio ($\mathcal{AR}$), for which it is known that the effects of tip vortices (TVs) become increasingly important. As a result, there is a complex interaction between the leading-edge separation region (LESR) and the TVs, which can affect the aerodynamic loads and flight characteristics.

A flight condition that is of considerable importance to low-$\mathcal{AR}$ wings is side-slip. This is because these types of wings are susceptible to instability caused by disturbances. For example, a side-slip condition can be easily induced in an energetic environment by a slight wind gust [6]. The complexity of low-$\mathcal{AR}$ vehicle control stems from the sensitivity of their lateral dynamics. The fact that low-$\mathcal{AR}$ wings have near-zero roll damping [4] amplifies the impact of roll moments produced by lateral flow asymmetries. While a planar low-$\mathcal{AR}$ rectangular wing is able to generate statically stable roll moments in side-slip (i.e. $C_{l,\beta} < 0$), the coupling between vortex lift and angle of attack results in an over-stabilizing dynamic derivative at increased angles of attack. Shields & Mohseni [4] showed that for rectangular wings of sufficiently small aspect ratio, such high levels of lateral stability, coupled with low roll damping, can result in an under-damped dutch-roll-like stability mode. Additionally, angle of attack disturbances with a frequency similar to this mode can result in a divergent modal response that they termed 'roll resonance', and which couples the longitudinal and lateral dynamics. The lateral component is similar to the well-known phenomenon of 'wing rock' observed to occur on free-to-roll delta wings [7,8] and to the self-induced oscillations of free-to-roll rectangular, elliptical, Zimmerman wings [9].

The majority of previous work on wings in side-slip has been applied to high aspect ratios or to slender delta wings [10–12]. In this regard, Shields & Mohseni have conducted research on low-$\mathcal{AR}$ rectangular wings in side-slip [13–15]. Their static measurements showed the presence of a few phenomena that they put under an umbrella term called 'roll stall'. In this manuscript, the term roll stall refers specifically to the sudden decrease of the roll moment magnitude that occurs at a particular angle of attack, prior to which there is a monotonic increase with α; this terminology is chosen based on the similar behaviour of the lift coefficient when lift stall occurs. The importance of roll stall on the flight dynamics of such a wing lies in the ability of a flight controller to accurately predict the actual control authority available. In other words, a linear controller will not be able to account for the rapid change in the $C_{l,\alpha}$ stability derivative associated with roll stall, and thus the wing could easily be sent into unstable flight. It should be noted that Levin & Katz [7] found a very similar roll stall behaviour for slender delta wings, where the roll stall event occurs *simultaneously* with the lift or normal force stall. This happens, because the vortex lift of slender delta wings is due only to the *two* vortices generated along the highly swept leading edges. However, inspection of the data of Shields & Mohseni reveals that, for rectangular wings, roll stall occurs well before lift stall for aspect ratios of unity and below. Moreover, low-$\mathcal{AR}$ rectangular wings are different from delta wings in that there are *three* main wing edges and corresponding vortices which interact to generate loads on the wing.

For delta wings, the aspect ratio is (by definition) uniquely determined from a single parameter, namely the sweep angle Λ of the leading edges. Hence, a low-$\mathcal{AR}$ delta wing is not necessarily geometrically representative of other low-$\mathcal{AR}$ wings that have more degrees of freedom in the planform definition. While the rolling dynamics of delta and rectangular wings, indeed, display similar traits, we believe that the different wing geometry is a fundamental difference that leads to different flow physics and interactions that are responsible for the roll characteristics. The main purpose of this paper is to investigate the high angle of attack flow features of low-$\mathcal{AR}$ rectangular wings in side-slip and to propose a simplified vortex model of the wings that incorporates these features.

Although considerable understanding on roll stall of rectangular wings has been gained, those studies used global measurements, namely force balance data. In this paper, we obtain local

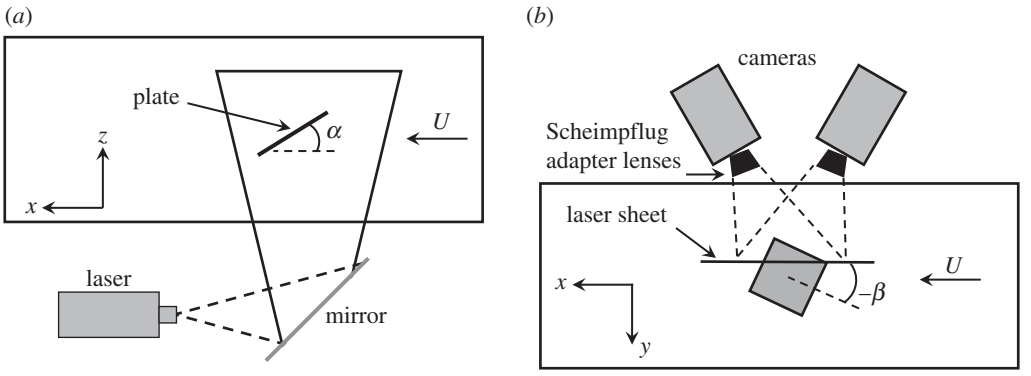

Figure 1. Schematic of the experimental set-up as viewed from the (*a*) side and (*b*) top of the wind tunnel test section. Also indicated are the freestream velocity U, the angle of attack α, the angle of side-slip $-\beta$ and the laboratory coordinate system x–y–z. The laser is located below the wind tunnel, and the laser sheet is turned up into the test section with a mirror. The cameras are tilted at the angle of attack of the plate.

measurements of the flow around low-$\mathcal{R}$ wings in side-slip via stereoscopic digital particle image velocimetry (S-DPIV) to provide a more quantitative exploration of various flow phenomena. The experimental observations will then be used to justify some assumptions in a simple model that predicts the lift, drag and rolling moment of the wings. For the experiment, a high angle of attack is chosen for two reasons: (i) roll stall occurs at relatively high angles of attack, 20–30° depending on aspect ratio and (ii) experimental investigations of this type are fewer when compared with those for small angle of attack for which the flow field has been well studied and the aerodynamic forces may be reasonably predicted. In regard to the latter point, the experiments will help identify how certain flow features, such as vortex circulations and locations, are altered at large incidences. Lastly, knowledge of the vortex topology can aid the design of future generations of MAVs to improve vehicle control and performance.

This paper is organized as follows. The experimental set-up is described in §2. In §3, the three-dimensional vortex structure is presented, followed by a simplified vortex skeleton representation. The vortex model is developed in §4 and is based on a new interpretation of a limiting form of slender body theory, as well as the leading-edge suction analogy of Polhamus [16]. The model is compared with direct force and moment measurements in §5, and for reference, the main model equations are collected in appendix A.

2. Experimental set-up

The experiments are performed in a recirculating wind tunnel manufactured by Engineering Laboratory Design, Inc. that has a cross section of $61 \times 61\,\mathrm{cm}^2$ and a test section length of 2.44 m. The wind speed range is 3–91 $\mathrm{m\,s^{-1}}$ with freestream turbulence intensity of 0.12%. A flat plate model of aspect ratio 1 is constructed from an acrylic sheet with thickness of 3.175 mm; the edges are left square. The chord and span are $c = b = 7.5$ cm, giving a thickness-to-chord ratio of 4.2%. With a freestream velocity of $U = 16.15\,\mathrm{m\,s^{-1}}$ the chord-based Reynolds number is about 80 000. Measurements are performed at an angle of attack of $\alpha = 35°$, and side-slip angles of $\beta = 0°$, 10°, 20° and 35°. These large side-slip angles are studied, because a typical MAV flight speed is approximately $10\,\mathrm{m\,s^{-1}}$ and with a gust speed range of 9–16 knots (4.6–8.2 $\mathrm{m\,s^{-1}}$), the approximate side-slip range would be $\beta \approx 25$–40°. The flat plate wings are mounted on a sting that is fixed to a linear motor, which allows the models to be translated in the cross-stream direction.

An S-DPIV system (figure 1) is used to measure the three-component velocity field within planes of the flow (2D-3C); the laser sheet is vertically coplanar with the streamwise direction of the wind tunnel. The mean volumetric flow field (3D-3C) is reconstructed from many closely

spaced data planes, which is accomplished by laterally translating the plate through the laser sheet; in the worst-case scenario, the wing is still about 2.5 chords from the tunnel walls. The wind tunnel is seeded with olive oil particles (approx. 1 µm) generated by an atomizer. Image pairs with an interframe time of $\Delta t = 50\,\mu$s are captured with 1 Mpx CMOS cameras (Phantom v.210/v.211, $1280 \times 800\,\text{px}^2$) and illumination of the particles is provided by a 200 mJ Nd:YAG laser (New Wave PIV Solo XT, $\lambda = 532$ nm). The object-to-image plane mapping function [17] of the S-DPIV system is determined with a precision-machined, dual-plane calibration target. Misalignment of the target with the laser sheet is corrected with the disparity map method [17–19], for which 50 images (of the undisturbed freestream) are used.

The cameras are tilted at the angle of attack, so that the plate appears horizontal in the images; this improves the data quality and yield near the plate, because the DPIV evaluation algorithm uses rectangular interrogation windows. For each plane of S-DPIV data, a set of 50 images are captured at a rate of 15 Hz (approx. 3.25 s acquisition time). An iterative multi-pass DPIV evaluation algorithm consisting of windowing shifting/deformation is performed on each image pair starting from a $40 \times 40\,\text{px}^2$ interrogation window to $20 \times 20\,\text{px}^2$ with 50% overlap. Finally, in each measurement plane, the three-component velocity vector (2D-3C) is reconstructed. The in-plane spatial resolutions are $\Delta x = \Delta y = 0.023c$, whereas the out-of-plane resolution is $\Delta z = 0.016c$, and is chosen based on the laser sheet thickness obtained from a burn paper measurement. The size of the measurement volume is then $2.52c \times 1.46c \times Zc$ in the x–y–z directions, where $Z = 1.6$–2 depending on β, and the number of vectors is $113 \times 66 \times K$, where $K = 100$–125, again depending on the slid-slip angle.

The theoretical ratio of the out-of-plane measurement uncertainty to that of the in-plane is $\delta w/\delta u = 1/\tan(\theta)$, where 2θ is the total angle between the cameras. In the experimental set-up, $2\theta \approx 55^\circ$, which gives $\delta w/\delta u \approx 1.92$. It is common to assume a $\delta p = 0.1$ px uncertainty level for typical DPIV evaluation algorithms [20], which can be converted to a velocity uncertainty as $\delta u = m\delta p/\Delta t$, where m is the scale factor of the image. For the current set-up $m = 168.785\,\mu\text{m px}^{-1}$ and so $\delta u/U = 0.021$. To obtain an *in situ* estimate of the standard error of the mean with 50 samples, the freestream measurements used for the disparity map were processed and analysed. Using these 50 temporal samples, the uncertainty at each S-DPIV measurement point is estimated as twice the standard deviation of the population. For the streamwise component, the maximum uncertainty observed in the measurement plane is $\max[\delta u/U] = 0.030$, whereas the spatial average is $\text{E}[\delta u/U] = 0.011$. For the vertical and out-of-plane components, the max/mean values are $\delta v/U = 0.029/0.010$ and $\delta w/U = 0.091/0.033$, respectively, and hence $\delta w/\delta u \approx 3$. These *in situ* estimates are larger than the theoretical/empirical ones as they account for the non-ideal conditions of the real set-up. Lastly, the max/mean uncertainties in the vorticity are $\delta\omega c/U = 0.796/0.292$, and are obtained from the local circulation method [21].

All position and velocity vectors are normalized by the chord, c, and freemstream flow, U, respectively. Accordingly, the vorticity is normalized by U/c. We define the laboratory coordinates to be such that the horizontal x-axis is pointing downstream, the y-axis is the cross-stream direction and the vertical z-axis is upward (figure 1). However, for some discussions, it will be convenient to represent quantities in the plate (or 'body') coordinates, for which the axes are coincident with the plate chord, normal and span.

3. Vortex structure

This section presents visualizations of the overall vortical structure, which are intended to familiarize the reader with the vortex topology and will help facilitate further discussions. The top row of figure 2 shows three-dimensional vorticity isosurfaces of the streamwise (ω_x) and cross-stream (ω_y) components (i.e. relative to the laboratory coordinates). We use the term 'upstream tip vortex' to refer to the structure that is created from the 'attacking' side edge; the term 'downstream tip vortex' refers to the opposite tip-edge vortex. In figure 2, these are the left/blue and right/red isosurfaces of columnar shape.

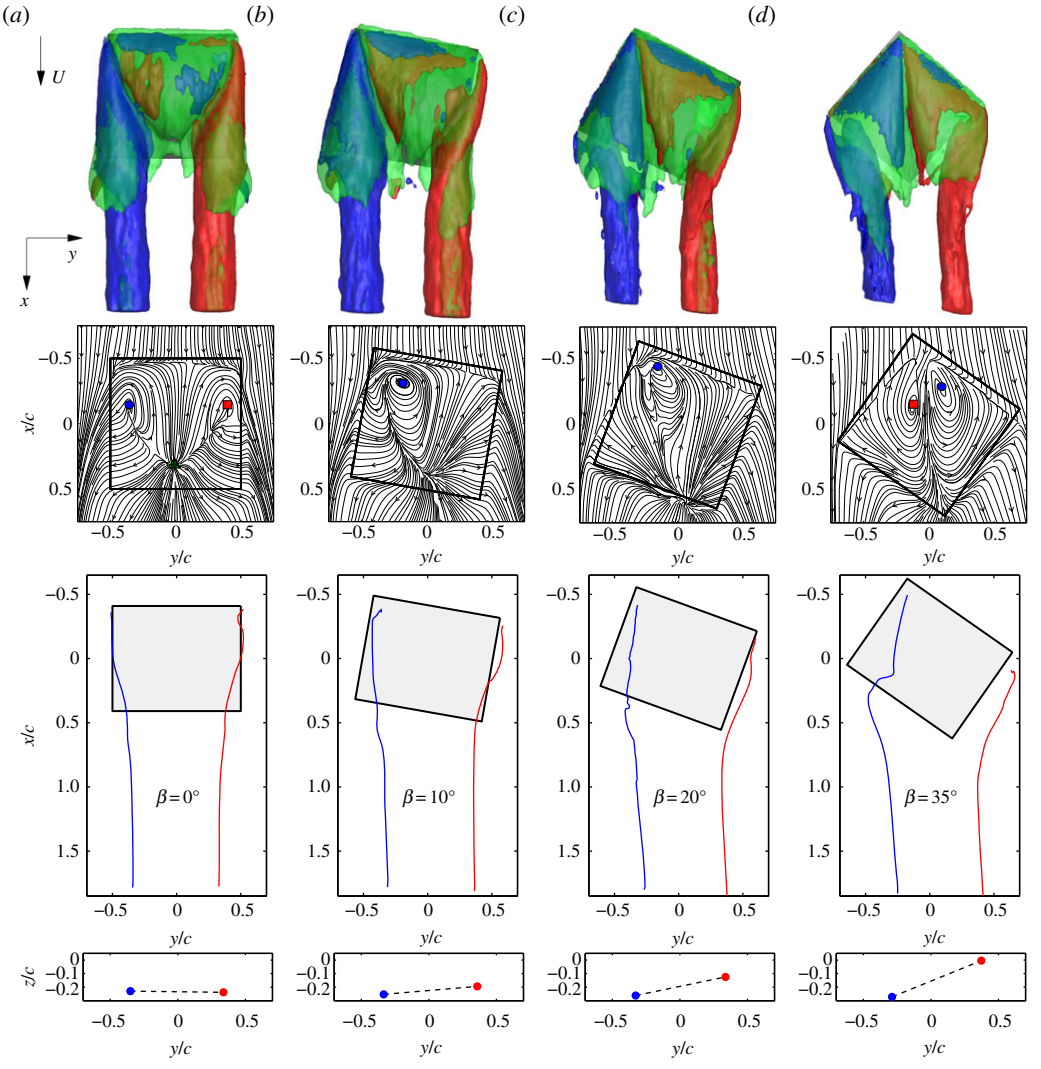

Figure 2. (Row 1) Vorticity isosurfaces: the components of the vorticity vector are relative to the lab coordinates (figure 1). Green, $\omega_y c/U = 3$ (LESR); red, $\omega_x c/U = 3$ (downstream TV) and blue, $\omega_x c/U = -3$ (upstream TV). The $\omega_y c/U$ isosurface is translucent to show the structures underneath. (Row 2) Streamlines in a plane located $0.023c$ above the plate surface. Solid symbols represent the locations of critical points in the flow. (Row 3) Streamwise vortex skeleton locations as a function of downstream distance; the projection of the plate is shown for reference. (Row 4) Vertical positions of the tip vortices in the wake at $x/c = 1$. The origin is at the plate centre. (*a*) $\beta = 0^\circ$, (*b*) $\beta = 10^\circ$, (*c*) $\beta = 20^\circ$ and (*d*) $\beta = 35^\circ$.

For $\beta = 0^\circ$, the familiar vortex structure consisting of left/right TVs and a LESR that has been reported by other researchers [1,22,23] is observed. In particular, Jian & Ke-Qin [24] (simulations/experiments for $Re = 10\,000$) and Tiara & Colonius [1] (computations for $Re = 300$) state that the strong downwash of the tip vortices acts to pin the LESR on the plate, thus allowing for reattached flow. This also appears to be the case for all side-slip angles of the current experiments. Hence, the tip vortex downwash seems to be a plausible mechanism for reattachment for a range of Re as well as for different wing geometries and orientations. Here, we refer to separated, but reattached flow as 'reattached flow', and when reattachment fails to occur we use the term 'massive separation'.

In the presence of side-slip, the wake is similar for each β. However, the vorticity over the plate changes more substantially with increasing β. Near the leading edge, the vortex sheets

from the upstream tip edge and the leading edge are comprised almost wholly of ω_y vorticity (green isosurface). These shear layers appear to 'blanket' the vortical structure and so represent a boundary-layer-like transition from the freestream velocity to the underlying vortex structures. The close proximity of the tip vortices results in a quick roll up of any trailing-edge vorticity before it can propagate far downstream. Because the tip vortices are formed along the wing tips, the near wake consists of columnar vortices that are already well into the roll-up process.

The second row of figure 2 plots streamlines in a plane located $\Delta x = 0.023c$ above the plate surface. For the $\beta = 0^\circ$ case, there is a streamline that makes a spatial distinction between the LESR and each TV. For $\beta \neq 0^\circ$, the distinction between the LESR and downstream TV becomes more ambiguous. At zero side-slip, three stagnation/critical points can be identified. The two points on the right and left are connected to a third point towards the trailing edge of the wing through two positive bifurcation lines [25,26]. As the side-slip angle increases, the right and rear critical points disappear from the wing resulting in the divergence and disappearance of the right bifurcation line, and by $\beta = 35^\circ$ another critical point on the left side of the wing appears and signifies a locally rotating flow opposite in sense to that associated with the original left critical point. In essence, the left and right critical points of the zero side-slip case have switched positions, the flow along the $z = 0$ line is reversed. These changes in the streamline topology indicate how a flow control device could alter the flow to perform a roll manoeuvre.

It is desirable to represent the vortex structure in figure 2 in a more simplified manner, and in particular, we are primarily concerned with the TVs. We identify a 'vortex skeleton' given by the position $\boldsymbol{x}_v$, and which is defined by vorticity-weighted centroids. The tip vortex locations are calculated using the streamwise vorticity (i.e. ω_x) in each x-plane of data to calculate the corresponding (y_v, z_v) coordinates. To 'track' each vortex and distinguish from other, nearby structures of the same sign vorticity, we use a clustering algorithm [27] that accumulates points in the vortex as determined by a thresholded vortex identification field. The circulation of the vortices is also computed in the process. Here, we are interested in the circulation generated by each wing edge, whether it be in a rotating vortex or a shear layer. Therefore, we define the side-edge shear layers to be part of the tip vortex structures, and we opt to use a vorticity magnitude threshold (rather than the Q-criterion, for example). The threshold value chosen was twice the uncertainty estimate in the vorticity, namely $\omega_{th} = 2\delta\omega \approx 1.2U/c$. The calculation was repeated with different threshold values, and it was found that around the chosen value, the vortex locations were not dramatically affected. The calculation does, however, have some difficulty near the leading edge where both the area of the tip vortices and their vorticity magnitudes are small.

The third row of figure 2 shows the cross-stream locations of the vortex skeleton (y_v) as a function of streamwise distance. These plots show a clearer distinction between the downstream TV and the rolled up and tilted portion of the leading-edge shear layer. The downstream TV remains mostly parallel to its respective tip edge until $\beta = 35^\circ$ where it begins separating away from the wing at the trailing edge. The upstream TV occupies more space over the wing as the side-slip is increased, but also remains nominally parallel to its edge. At $\beta = 35^\circ$, the upstream TV and the tilted, rolled-up portion of the leading-edge shear layer resemble the well-known leading-edge vortices of (non-slender) delta wings [28]. After a short distance into the wake, the cross-stream locations of both tip vortices remain essentially straight.

The fourth row of figure 2 plots the vertical vortex locations (z_v) at the plane $x/c = 1$ in the wake. This shows that with increasing side-slip the downstream TV is shed at a higher location into the wake, whereas the upstream TV positions are almost the same. As such, the wake vortex structure becomes more tilted, which indicates a total torque in the vortex structure that represents some contribution to the rolling moment on the wing.

4. Vortex model

In this section, we aim to develop a simple vortex model to predict aerodynamic loads and moments, with the angle of attack, side-slip angle and aspect ratio as variables. There are many successful aerodynamic models and relations for finite wings that already exist, such as

the collected works of Prandtl *et al.* [29], Bollay [30], Falkner [31], Jones [32], Helmbold [33], Küchemann [34], Brown & Michael [35], Mangler & Smith [36], Polhmaus [16], Lamar [37] and several extensions of these models. Some models are based on slender body theory, but several others employ lifting surface methods (e.g. Multhopp [38]) with three-dimensional spanwise and chordwise loadings. Some of the simpler existing models that rely on slender body theory usually have an elliptical spanwise lift distribution. For example, the pointed slender wing model of Jones [32] assumes a two-dimensional cross-plane flow at each chord position, and it is shown that this flow is characterized by an elliptical loading distribution across the local span. In this way, that model is limited to low angles of attack (as well as aspect ratios of course). More involved models use expansions to improve the range of applicability of the model, as well as to include relations for vortex positions and strengths. The leading-edge suction analogy of Polhamus, which was extended by Lamar, provides a nonlinear relation between forces and the angle of attack that has been shown to be accurate at high incidences. However, as pointed out by Riley & Smith [39], the Polhamus method does not offer insight on the actual separated flow structures; in turn, they developed a model that incorporates these features and yields results comparable to a slender body theory [40].

Given the vast amount of previous work, we do not intend to build up to these models, but rather to use their common features and results as inspiration to an oversimplified representation of the wing and vortex structure that bypasses some of the flow details addressed in the more sophisticated approaches. The novelty of our proposed model is to adopt the nonlinear vortex suction relation with the angle of attack of the Polhamus method and to represent the separated flow structures by line vortices with prescribed circulation distributions that are characteristic of large angles of attack, thus extending the range of applicability while circumventing the specification of more detailed information of the flow features. As such, a lifting surface calculation is not needed nor used. To make the model as simple as possible, the number of free parameters is kept to a minimum. The circulation distributions are determined from a new interpretation of a limiting slender-body-based potential flow model developed next in §4a and other assumptions about the vortex system are supported by the experimental findings of the previous sections.

In classical lifting line theory, the flow is potential in the sense that it remains attached to the wing. Hence, the circulation around the wing is equal to the circulation of the tip vortices as a consequence of the Helmholtz law of persistence of irrotationality. For wings with separated but reattached flow there is an additional circulation distribution associated with the separation region. However, the vortex lines that represent this leading-edge separation region begin and end on the wing and thus have an 'image' inside the wing that satisfies the Helmholtz law. Furthermore, they can be considered as *bound vortices*, because the LESR moves with the wing. Consider a wing that has established a reattached flow as illustrated in figure 3. The circulation representing the LESR is Γ_{le} and that of the tip vortices in the wake after the roll-up process is Γ_{w}. The total or effective bound circulation (owing to reattachment) is Γ_o and is related by $\Gamma_o = \Gamma_{\mathrm{le}} + \Gamma_{\mathrm{w}}$. Note that Γ_{le} cannot be determined independently, say by experiment, but may be found by knowledge of Γ_o and Γ_{w}, both of which can be measured. The circulation of the side-edge vortices Γ_{se} forms along the wing tip edges, and rolls up the vorticity, with circulation Γ_{te}, shed from the trailing edge. After the roll-up process completes, the circulation of the wake tip vortices is $\Gamma_{\mathrm{w}} = \Gamma_{\mathrm{se}} + \Gamma_{\mathrm{te}}$. Next, we begin with determining the different loading/circulation distributions. The model also requires determination of the downwash on the vortex system, and will be found subsequent to the circulation. The results are then substituted into equations of the Polhamus method and the remaining parameters are determined by matching limiting behaviours with α and $\mathcal{AR}$ to those predicted by existing, well-established models.

(a) Spanwise loading

In general, the cross-stream vorticity distribution is three-dimensional. Here we address the spanwise loading by appealing to slender body theory. Although it may seem strange to consider

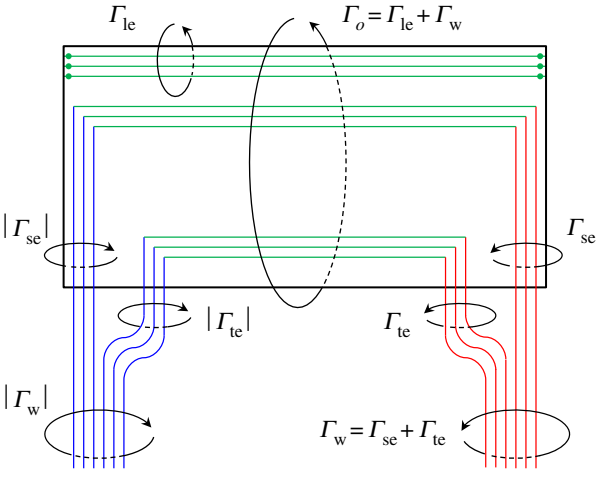

Figure 3. Schematic shows the circulations associated with a finite wing with reattached flow. Γ_o is the effective bound circulation, Γ_{le} is the circulation of the vortices representing the LESR; the dots represent that they are bound to the wing. Γ_{te} is the circulation shed at the trailing edge, Γ_{se} is the circulation shed at the side edges (wing tips) and Γ_w is the circulation of the fully formed wake vortices. (Online version in colour.)

this limit for the *spanwise* loading distribution, it will be shown that interesting results are obtained. As such, we have technically already made the assumption that the cross-stream vorticity distribution is confined to the wing surface: $\omega_y = \omega_y(x, y)$. The physical implications of this will be interpreted shortly. The variable x is now taken to represent the distance from the leading edge as opposed to locating the centre of the plate as in the experimental portion of this paper. For models of low-$\mathcal{AR}$ wings, it is often assumed [34] that this $\omega_y(x, y)$ distribution is a separable product of functions, $\omega_y(x, y) \propto \gamma_x(x)\gamma_y(y)$, where the spanwise distribution of cross-stream vorticity is γ_y. Under the assumptions of slender body theory, Bernoulli's equation gives

$$p - p_\infty = -\rho U \phi_x - \frac{\rho}{2}[\phi_y^2 + \phi_z^2], \tag{4.1}$$

where p is the pressure and ϕ is the potential with subscripts indicating differentiation with respect to that variable. In Jones' [32] pointed wing model, it is supposed that the increase of the wing span with downstream distance is responsible for ϕ_x via a corresponding increase of added mass to be accelerated. Here, we investigate a slender wing and instead explicitly account for side-edge vortices and their streamwise-dependent circulation $\Gamma_x(x)$, and hence ϕ_x will be non-zero even if the local span variation is negligible, e.g. a *rectangular* wing. However, slender span variation effects can be included by adding $\phi' = \phi'(b(x))$ to the total potential. Note that ϕ' cannot be used to model a rectangular wing in side-slip, because this 'pointed wing' has an apex angle of 90° (i.e. the rectangular corner angle) and violates the slender body assumptions.

We then consider the situation of $\mathcal{AR} \to 0$ by the limit $b \to 0$, which is depicted in figure 4 and shows the two long side-edge vortices that will dominate the flow. Note that Jones [32] does not explicitly consider this limit, but only implicitly through the use of slender body theory. Applying this limit before integrating Bernoulli's equation is a major difference in our approach, but we will show that the results are consistent with the lifting surface calculations of Polhamus and Lamar. As $b \to 0$, then $\phi' \to 0$, and the two side-edge vortices merge into a vortex doublet of strength $\lambda \equiv b\Gamma_x$, for which the potential is

$$\phi = \Gamma_x \frac{\tilde{z}}{\pi[\tilde{y}^2 + \tilde{z}^2]} \equiv \Gamma_x \tilde{\phi}, \tag{4.2}$$

where $\tilde{z} \equiv 2z/b$, $\tilde{y} \equiv 2y/b$ are non-dimensional scaled coordinates. Figure 4 also plots the experimental measurement of the corresponding flow for the $\mathcal{AR} = 1$ wing at two chordwise

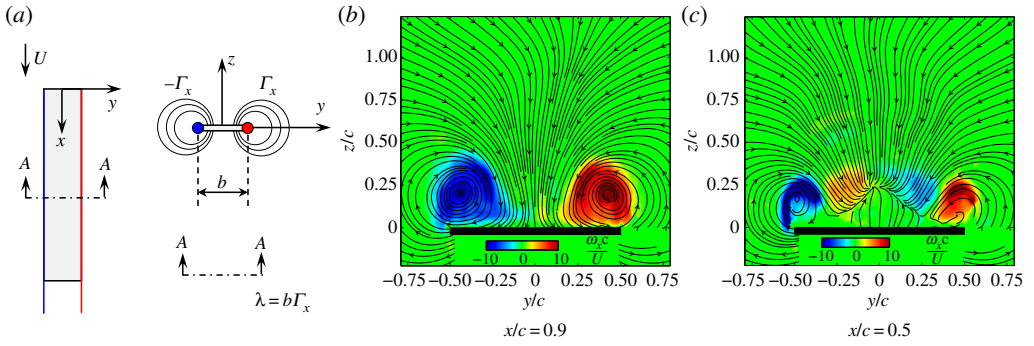

Figure 4. (*a*) Schematic of the $\mathcal{AR} \to 0$ limiting case for a rectangular wing. The side-edge vortices have variable circulation $\Gamma_x(x)$ and as the span $b \to 0$ the two coalesce into a vortex doublet of strength $\lambda = b\Gamma_x$. (*b*) Measured streamwise vorticity field $\omega_x c/U$ and streamlines of the tip vortex flow for the $\mathcal{AR} = 1$ wing in a plane near the trailing edge (middle) and at the centre of the plate (right). Here, x/c is the distance from the leading edge. (Online version in colour.)

locations on the wing and shows that the flow outside the LESR is quite similar to the vortex doublet/dipole flow despite that $\mathcal{AR} = 1$ is not necessarily a small value in the limiting sense. The physical interpretation of this is that, outside of the LESR, the cross-plane flow is potential-like and is dominated by the tip vortices. This is obviously in contrast to the $\mathcal{AR} \to \infty$ limit where the flow is in a streamwise plane and is dominated by a spanwise vortex monopole (i.e. the leading-edge vortex). Note that without multiplication with b, then Γ_x is technically infinite in the vortex doublet solution. However, this is a result of assuming ω_y to be bound to the wing surface, as mentioned at the beginning of this subsection. More specifically, because we are considering reattached flow, then it requires an infinite strength of the side-edge vortices to suppress the separated vorticity back into the wing. Obviously, this is not the reality of the situation, but is a limiting, idealized representation of the Γ_x flow bounding ω_y to the wing.

Substituting equation (4.2) into equation (4.1), it is found that

$$p - p_\infty = -\rho U \tilde{\phi} \frac{\mathrm{d}\Gamma_x}{\mathrm{d}x} - \frac{\rho}{2}\left(\frac{2\Gamma_x}{b}\right)^2 \frac{\tilde{\phi}^2}{\tilde{z}^2}. \tag{4.3}$$

To evaluate the pressure on the wing surface, we must take $z = 0$ and $y \in [-b/2, b/2]$, however, because we have also used the vortex doublet potential then $b \to 0$. Therefore, $\tilde{z}$ and $\tilde{y}$ are allowed to asymptote to non-zero values in the limit; these variables are essentially inner variables as are used in perturbation methods [41]. We want to choose the scale, so that we can still 'see' the spanwise effects and variations. For $\tilde{y}$, it is obvious that it should behave the same as y and range linearly across the span. However, because $z \equiv 0$ represents the surface of the wing, then in order to have $\tilde{z} = O(1)$ in the limit, this means that $\tilde{y} \in [-\infty, \infty]$. Physically, we have scaled our coordinates, so that we can 'see' between the vortex doublet where the wing is located and consequently the wing tips are at infinity. The value of $\tilde{z}$ must change sign in going from one side of the wing to the other in order for lift to be generated. As such, from equations (4.2) and (4.3), the pressure difference across the lower and upper surfaces of the wing is then

$$\Delta p = p_\mathrm{l} - p_\mathrm{u} = 2\rho U |\tilde{\phi}| \frac{\mathrm{d}\Gamma_x}{\mathrm{d}x}, \tag{4.4}$$

where the absolute value of $\tilde{\phi}$ reflects the sign change in $\tilde{z}$ across the wing surface. Although the pressure term containing $\tilde{\phi}^2/\tilde{z}^2$ does not contribute to the total lift directly, it is an important feature of the flow. This pressure is the dynamic pressure induced by the vortex doublet (recall equation (4.1)), or equivalently, the side-edge vortices and physically represents the tip vortex downwash that reattaches the leading-edge shear layer. The second chordwise location of the experimental flow field plotted in figure 4 cuts through the LESR and clearly shows that the

potential flow outside the LESR acts to promote reattachment. Hence, this analytical expression could be employed to predict lift stall.

Returning to Δp, we can integrate along the chord, which assuming the side-edges vortices to have zero circulation at the leading edge, then gives the spanwise loading distribution:

$$\int \Delta p \, \mathrm{d}x = 2\rho U |\tilde{\phi}| \Gamma_{\mathrm{se}}, \tag{4.5}$$

where $\Gamma_{\mathrm{se}} = \Gamma_x(x = c)$ is the fully developed circulation of the side-edge vortex. Much in the way that Jones' result for the spanwise lift distribution is independent of planform, the above result is independent of $\Gamma_x(x)$. Also, note that while the chord c should be large enough for equation (4.1) to apply, we have not taken $c \to \infty$ to make $\mathcal{AR} \to 0$.

Because we are assuming reattached flow, the dependence of the forces on angle of attack is represented by the trigonometric terms in the Polhamus method (see equation (4.17) in §4e). In other words, the integration of the spanwise loading distribution in equation (4.5) would give the lift-curve slope, say L_α, in the case of $\mathcal{AR} \to 0$; the result of this is

$$L_\alpha = \int 2\rho U \tilde{\phi} \Gamma_{\mathrm{se}} \, \mathrm{d}y = \rho U b \Gamma_{\mathrm{se}} \int_{-\infty}^{\infty} \tilde{\phi} \, \mathrm{d}\tilde{y} = \rho U b \Gamma_{\mathrm{se}}, \tag{4.6}$$

and it should be noted that this is *independent* of the value of $|\tilde{z}|$, because the limits on the integral are from positive to negative infinity and $\tilde{z}$ is finite. Now, consider a rectangular wing and a delta wing whose maximum spans and root chord lengths are equal, so that the rectangle of area $S = bc$ is the bounding box on the delta wing of area $S_\Delta = bc/2$. This best isolates the sweep angle effects by creating an equal competition between the planform area and aspect ratio ($\mathcal{AR} = b/c$ versus $\mathcal{AR}_\Delta = 2b/c$). Nonetheless, the above result should be consistent with that of Jones, which is $C_{L_\alpha} = (\pi/2)\mathcal{AR}_\Delta = \pi\mathcal{AR}$. The meaning of this is that, while Jones' lift-curve slope is valid for all slender wings, including delta and rectangular wings, it is so for different numerical ranges of $\mathcal{AR}$. For rectangular wings the value of $\mathcal{AR}$ must be comparably smaller, because the assumption of slenderness is violated otherwise; this effect of wing geometry is a fundamental difference between delta and rectangular wings. For example, an $\mathcal{AR}_\Delta = 1$ delta wing has a sweep angle of $\Lambda \approx 76^\circ$ and is therefore slender. However, an $\mathcal{AR} = 1$ rectangular wing is not necessarily slender and because $\mathcal{AR} = b/c$ this obviously represents the middle ground of when spanwise and chordwise dimensions are equally important. Therefore, the range of numerical values of $\mathcal{AR}$ for which Jones' result is valid for rectangular wings is then half that of a comparable delta wing.

Non-dimensionalizing equation (4.6) and equating it to the result that $C_{L,\alpha} = \pi\mathcal{AR}$ gives

$$\frac{\rho U b \Gamma_{\mathrm{se}}}{(1/2)\rho U^2 S} = \frac{2\Gamma_{\mathrm{se}}}{Uc} = \frac{2\Gamma_{\mathrm{se}}}{Ub}\mathcal{AR} = \pi\mathcal{AR} \;\; \rightarrow \;\; \frac{2\Gamma_{\mathrm{se}}}{Ub} = \pi. \tag{4.7}$$

In §4e, where we apply the Polhamus method, it will be seen that the right-most term in equation (4.7) is equivalent to the coefficient of the vortex force constituent (i.e. $K_{\mathrm{v,se}}$) as $\mathcal{AR} \to 0$. Furthermore, the right-hand side, namely π, is exactly the value computed by Polhamus [16] via a lifting surface method for delta wings as $\mathcal{AR} \to 0$. The same value was computed by Lamar [37] for rectangular wings with a modified method and using impulsive chordwise loading and elliptical span loading. Lamar explained that the reason the two limiting values are the same is because the leading edges of the delta wing become like the side edges of a rectangular wing as $\mathcal{AR} \to 0$. Thus, our model is an interpretation of the Jones slender wing model for rectangular wings and which analytically predicts the correct behaviour in the zero-aspect-ratio limit.

Lastly, we revert back to the spanwise loading distribution, which is proportional to the spanwise circulation distribution, γ_y, which, in turn, is proportional to $\tilde{\phi}$. In order to find what form this distribution takes, we need to find a value for $\tilde{z}$ and one that has physical meaning. The expression for the spanwise velocity $v = \phi_y$ shows that in order for this component to be physically consistent with a flow going around the tip from the lower to upper side then $\tilde{z} < 0$; note the exclusion of $\tilde{z} = 0$, which returns the degenerate case of a singular pressure at the origin. Although each velocity is finite, continuous and differentiable, we now satisfy a Kutta-like

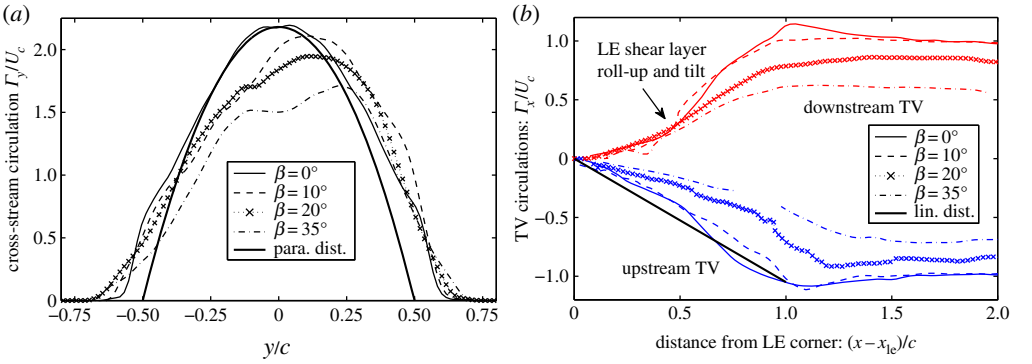

Figure 5. (*a*) Cross-stream circulation distribution. (*b*) Tip vortex circulations as a function of downstream distance from the respective leading edge (LE) corner x_{le}. For the upstream TV of the $\beta = 35^\circ$ case, a continuous vortex location could not reliably identified near the trailing edge where the structure rapidly transitions from a columnar wake vortex to a vortex connected to a shear layer (e.g. the Mangler & Smith [36] vortex sheet model). These data are omitted from the figure, but the trend is clear nonetheless. (Online version in colour.)

condition of zero velocity at the wing tips. It is found that $v = 0$ only at $\tilde{z} = 0$, which is not in the acceptable range. If we consider that a real, finite-span wing has wing tips at $y = b/2$, then taking $\tilde{y} = 1$, we find that $w = 0$ at $\tilde{z} = -1$. Physically, we can interpret this to mean that the wing resides below the side-edge vortices, which is clearly the case (e.g. figure 4). Furthermore, if the flow were to separate at the wing tip, as it does in a real flow, then it would do so tangentially to the wing, because $w = 0$ and $v \neq 0$. Therefore, assigning $|\tilde{z}| \equiv 1$ the spanwise circulation distribution is

$$\gamma_y(y) \propto \tilde{\phi} = \frac{1}{1+\tilde{y}^2} = 1 - \tilde{y}^2 + O(\tilde{y}^4), \tag{4.8}$$

which is nearly the equation of parabola (except very near the wing tips). The experimental measurement (S-DPIV data) of the circulation corresponding to cross-stream vorticity (i.e. ω_y) is plotted in figure 5*a*. These distributions validate the parabolic shape suggested by equation (4.8). While the integrated difference between our $\mathcal{AR} \to 0$ model and that of Jones' is only a factor of $\frac{1}{2}$, the geometry and physics involved are very different because of the broad-facing leading edge of rectangular wings. The meaning of this relation is that wings with a broad-facing leading edge, and which achieve reattachment via a tip vortex dominated flow (e.g. low-$\mathcal{AR}$ rectangular wings), will establish a parabolic distribution at higher angles of attack owing to circulation of the reattached LESR, rather than an elliptic distribution of classical aerodynamics.

Based on the above result and the experimental validation from the S-DPIV measurements (figure 5*a*), for our vortex model with finite-$\mathcal{AR}$ wings, we employ the following relation for the spanwise circulation distribution:

$$\gamma_y(y) = \Gamma_o \left[1 - \frac{y^2}{y_1^2}\right], \tag{4.9}$$

where $b_{\text{eff}} = 2y_1$ is the *effective span* of the cross-stream circulation distribution and is the distance between the outermost wing tips; for $\beta = 0$ it is simply $b_{\text{eff}} = b$.

(b) Side-edge vortex circulation

Here, the potential flow model developed in the previous section (equation (4.2)) is used to find the circulation distribution of the forming side-edge vortices, $\Gamma_x(x)$. These vortices will cause a vortex suction force in the sense of Polhamus' method, i.e. one that is proportional to $\sin^2\alpha$. Because the real velocity on the plate surface should be zero, we can interpret the value of $v = \phi_y$

near the wing tip to be the strength of a shed vortex sheet that generates the side-edge vortex

$$v = \frac{\mathrm{d}\Gamma_x}{\mathrm{d}x} = \Gamma_x \frac{2\tilde{\phi}_{\tilde{y}}}{b}, \tag{4.10}$$

with the second equality coming from equation (4.2). The exponential solution of this first-order differential equation cannot satisfy the condition that $\Gamma_x(0) = 0$. This is not surprising, because this location is the corner of the wing where the two-dimensional assumption of slender body theory is invalid. However, if we assume that this represents the tip vortex growth rate downstream of the leading edge, then after expanding the exponential we obtain

$$\frac{\mathrm{d}\Gamma_x}{\mathrm{d}x} \sim \frac{2\tilde{\phi}_{\tilde{y}}}{b} + O(x), \tag{4.11}$$

and indicates a constant growth rate or a linear growth of $\Gamma_x \sim x$. This near linear growth is also the trend obtained by some of the simpler slender body wing models [39,40]. Hence, for our model, we now assume that each side-edge vortex has

$$\Gamma_x(x) = \Gamma_{\mathrm{se}} \frac{x}{c}, \tag{4.12}$$

where x is the distance from the respective leading-edge corner along the chord for the case of side-slip. This expression is further supported by our experimental measurements of the side-edge vortex circulations, which are shown in figure 5*b*. Moreover, figure 5 shows that the circulation magnitudes maintain a nominally constant value in the wake, and that these values are the same for each TV. With increasing side-slip the circulation values decrease, which is the same trend for the LEVs of a delta wing as the sweep angle is increased [42]. Closer observation of the experimental circulations shows that the downstream TV experiences two different growth rates. From the leading edge the first growth rate is slower, when compared with the upstream TV. However, at around the mid-chord location, the rolled-up and tilted portion of the leading-edge shear layer begins to feed into the downstream TV and constitutes the second growth rate phase, which is comparable to the rate of the upstream TV. However, the circulation differences are minor, and we ignore this effect in our model.

(c) Chordwise loading

For low-$\mathcal{AR}$ wings whose aspect ratios are of order unity, the total chordwise loading will obviously depend on the distribution of cross-stream vorticity, $\omega_y(x, y) = \gamma_x(x)\gamma_y(y)$, and not just the circulation of the side-edge vortices, $\Gamma_x(x)$, of the previous section. It is often assumed that $\gamma_x(x)$ is impulsive, constant or has the 'flat-plate' distribution [34] also called the '$\cot(\theta/2)$' distribution [37], which is given by $\gamma_x \sim \sqrt{(1 - x/c)/(x/c)}$. When integrated over the chord this gives a resultant force proportional to $\pi/2$ that acts at the quarter-point from the leading edge. In a real flow, obviously, the loading will not be impulsive. Figure 6*a* shows the 'flat-plate' and constant loadings along with the chordwise distribution of the experimental cross-stream vorticity averaged over the span of the $\mathcal{AR} = 1$ plate. Near the leading edge the experimental γ_x shows a rapid increase to a somewhat constant value and then decreases in a fashion similar to the flat plate distribution. Therefore, it appears the experimental data have features of both the 'flat-plate' and constant loading types and we now assume that the chordwise loading in our model is a combination of the two. As a result, the integrated effect of this distribution is still a force proportional to $\pi/2$, but which acts somewhere between the quarter-chord and mid-chord points, because the constant loading acts at the mid-chord. Therefore, $\omega_y = (\pi/2)\gamma_y(y)$, where the $\pi/2$ factor will later be absorbed into γ_y for convenience.

(d) Downwash

In the Polhamus method, the vortex forces are affected by the downwash on the vortex system, which we now compute using the specified the circulation distributions. Recall that the spanwise

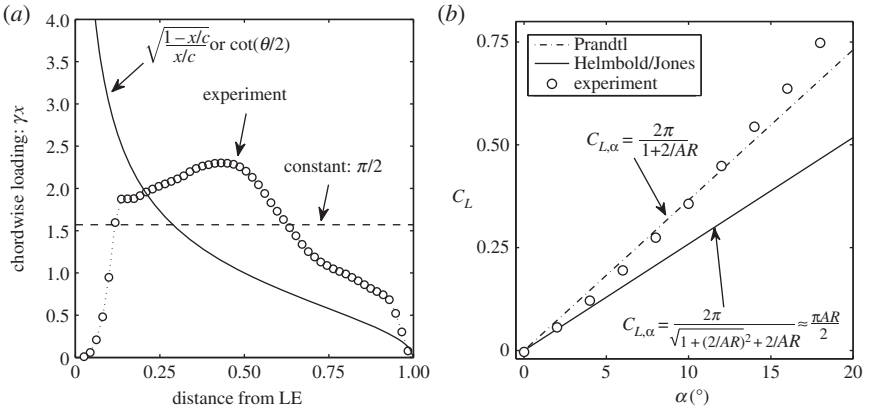

Figure 6. (*a*) Plot of chordwise loading of spanwise vorticity as a function of distance from the leading edge (LE) for the 'flat-plate' or $\cot(\theta/2)$ distribution and constant loading. The experimental data are the chordwise distribution of spanwise vorticity ω_y. (*b*) Comparison of experiment to lifting line theory with lift-curve slopes from the Prandtl and Helmbold equations; the asymptotic behaviour of Helmbold's equation is Jones' lift-curve slope.

circulation distribution in this model is given by $\Gamma_o(1-y^2/y_1^2)$ (see equation (4.9)), which was derived from the slender body potential flow model in §4a. Following the derivation of Prandtl's lifting line theory given in Milne–Thomson [43], consider two circuits C and C' that pass around the wing at the spanwise locations of η and $\eta + \mathrm{d}\eta$. The circulations around these circuits are Γ_η and $\Gamma_\eta + \mathrm{d}\Gamma_\eta$. Usually, $-\mathrm{d}\Gamma_\eta$ is described as the differential amount of circulation shed into a vortex sheet at the trailing edge. According to the relation $\Gamma_o = \Gamma_{\mathrm{le}} + \Gamma_{\mathrm{w}}$, the vortex sheet shed at the trailing edge does not have a total circulation Γ_o, because Γ_{le} remains bound to the wing. Therefore, the differential amount of shed circulation is $-\mathrm{d}\Gamma_{\eta,\mathrm{te}}$ (figure 3). Then, assuming that the distribution of shed vorticity is proportional to Γ_η, namely $\Gamma_{\eta,\mathrm{te}} = \Gamma_{\mathrm{te}}(1-\eta^2/\eta_1^2)$, then the differential *downwash* velocity induced at a spanwise point y by the (semi-infinite) line vortex at η is $\mathrm{d}w_{\mathrm{te}} = -\mathrm{d}\Gamma_{\eta,\mathrm{te}}/[4\pi(\eta - y)]$. The circulation distribution can be written as $\Gamma_\theta = \Gamma_{\mathrm{te}} \sin^2\theta$. Letting $\eta = -y_1 \cos\theta$ and $y = -y_1 \cos\phi$, then upon substitution and integrating, we obtain

$$w_{\mathrm{te}}(\phi) = \frac{1}{4\pi}\int_0^\pi \frac{2\Gamma_{\mathrm{te}} \sin\theta\cos\theta\,\mathrm{d}\theta}{y_1(\cos\theta - \cos\phi)} = \frac{\Gamma_{\mathrm{te}}}{2\pi y_1}\left[2 + \cos\phi \log\left(\frac{1-\cos\phi}{1+\cos\phi}\right)\right] \tag{4.13}$$

and

$$w_{\mathrm{te}}(y) = \frac{\Gamma_{\mathrm{te}}}{2\pi y_1}\left[2 + \frac{y}{y_1}\log\left(\frac{1-y/y_1}{1+y/y_1}\right)\right]. \tag{4.14}$$

Now, owing to the finite aspect ratio of the wing, the tip vortices form along the side edges of the wing and grow to a value of Γ_{se} at the trailing edge (recall figures 2 and 5). Therefore, there is an additional downwash on the wing owing to the side-edge/tip vortices. For simplicity, we first assume that the tip vortex system resides in the plane of the wing; this is the same assumption as in lifting surface methods used in the work of Polhamus and Lamar. Second, the side-edge vortices are assumed to remain parallel to their respective side edges. The downwash of this system is then normal to the wing. Lastly, we neglect the induced velocity from the growing portion of the side-edge vortex on the wing and consider the effect of Γ_x to be equal to a semi-infinite line vortex extending downstream from the trailing edge at the wing tip. For moderate side-slip angles, these latter two assumptions are supported by the vortex skeleton locations shown in figure 2, but their validity will weaken with increasing side-slip as the vortices begin to move further away from their respective side edges. The downwash accounting for both tip

vortices is then simply

$$w_{se}(y) = \frac{\Gamma_{se}}{2\pi}\left[\frac{1}{y_1+y}+\frac{1}{y_1-y}\right] = \frac{\Gamma_{se}}{2\pi y_1}\left[\frac{1}{1-y^2/y_1^2}\right] = \frac{\Gamma_{se}\Gamma_o}{2\pi y_1}\left[\frac{1}{\gamma_y(y)}\right]. \tag{4.15}$$

Equation (4.15) is interesting insofar as the side-edge vortex-induced velocity (i.e. between two semi-infinite line vortices) is not directly dependent on our particular choice of γ_y as a parabola. However, the limit of these two vortices approaching each other is the vortex doublet, which was used in deriving the spanwise circulation distribution. Clearly, this downwash is not constant along the span as it is for Prandtl's lifting line theory, but rather it will result in a constant vortex force distribution along the span, because this force is proportional to $w_{se}\gamma_y$.

Obviously, the downwash velocities are each singular at the wing tips and at a small distance $\xi = |y_1 - y|$ from the wing tip, we have

$$w_{se} + w_{te} \sim \frac{\Gamma_{se}}{4\pi\xi} - \frac{\Gamma_{te}}{2\pi y_1}\log\left[\frac{\xi}{y_1}\right]. \tag{4.16}$$

Therefore, the velocity at the trailing-edge corners can be non-singular, namely zero, only if Γ_{te} is infinitely larger than Γ_{se}. That this condition cannot be satisfied seems unavoidable, because when the trailing-edge vorticity rolls up into the side-edge vortices the total wake vortex circulation, Γ_w (figure 3), will be $\Gamma_w = \Gamma_{se} + \Gamma_{te}$ and it is clear that for low-$\mathcal{R}$ wings that Γ_{se} obtains a significant portion of Γ_w by the trailing edge. In other words, if $\mathcal{R}$ is sufficiently low, then the side-edge vortices quickly roll up any vorticity shed from the trailing edge meaning that $\Gamma_{se} \approx \Gamma_w$, and the near wake consists of the well-formed columnar tip vortices; this feature is observed in the current experiments (recall figures 2 and 5*b*). Nevertheless, we content ourselves with the singularity by recalling that the circulation γ_y is zero at the wing tips and thus the associated induced force will be finite.

(e) Potential and vortex forces

Here, we employ the method of Polhamus [16] to determine the potential and vortex suction forces that act normal to the wing surface. We assume the reader is familiar with the concept of this method and refer those that are not to the original paper. The force coefficients are normalized by $1/2\rho U^2 S$, where S is the planform area, which is $S = bc$ for the rectangular wings. The expressions for the force coefficients are

$$C_N = K_p \sin\alpha\cos\alpha + K_v \sin^2\alpha \;\rightarrow\; C_L = C_N\cos\alpha, \quad C_D = C_N\sin\alpha. \tag{4.17}$$

The coefficients K_p and K_v represent the potential and vortex constituents. The potential force is obtained from integration of $\gamma_y = (\pi/2)\Gamma_o(1 - y^2/y_1^2)$ across the effective span $b_{eff} = 2y_1$, where the $\pi/2$ factor represents the integrated effect of the chordwise loading (see §4c). The result is

$$K_p = \frac{2\pi}{3}\frac{\Gamma_o}{Uc}\frac{b_{eff}}{b}. \tag{4.18}$$

Next, following Lamar, we write $K_v = K_{v,le} + K_{v,se}$, where the first term represents the vortex suction force associated with the leading-edge circulation, and the second term represents the side-edge vortex force. The leading-edge vortex force is affected by the downwash of the wake vortex system (trailing-edge vorticity and side-edge/tip vortex), namely $w_{te} + w_{se}$. Again integrating across the effective span gives

$$K_{v,le} = K_p\left[1 - \frac{3}{2\pi\mathcal{R}}\frac{b}{b_{eff}}\left(\frac{\Gamma_{te}+\Gamma_{se}}{Uc}\right)\right] = K_p\left[1 - \frac{3}{2\pi}\frac{\Gamma_w}{Ub_{eff}}\right]. \tag{4.19}$$

where the second equality comes from the relation $\Gamma_{te} + \Gamma_{se} = \Gamma_w$ (recall figure 3*a*).

The side-edge vortex force is obtained by integrating Γ_x along the chord. We assume that the side-edge vortices do not experience a downwash from the cross-stream circulation. The reasoning behind this is that the downwash of the tip vortex system is largely responsible for the reattached flow and thus the latter would not exist without the former. We considered a

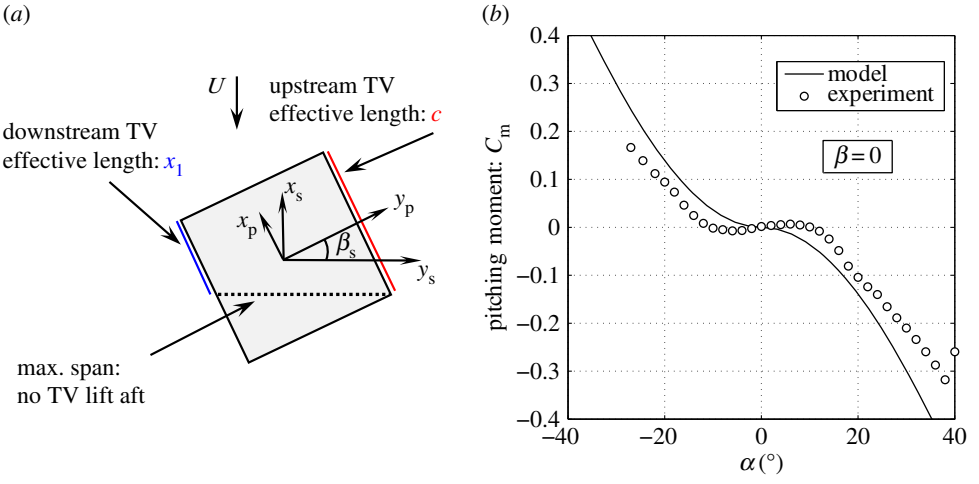

Figure 7. (*a*) Schematic shows the line of maximum span line aft of which no lift occurs from the TVs. The upstream TV has an effective length of the chord; the downstream TV has an effective length of $x_1/c = 1 - \mathcal{R}\tan\beta$. Also shown are the definitions of the $x_s - y_s$ and $x_p - y_p$ axes and the angle β_s. (*b*) The pitching moment coefficient as a function of angle of attack for the $\mathcal{R} = 1$ wing at zero side-slip. (Online version in colour.)

mutual downwash on each side-edge vortex from the other, but it was found that this results in a negligible reduction of their vortex suction force.

In the case of side-slip, the side-edge vortices should contribute asymmetrically to the force. Although we have fixed the side-edge vortices to the tip edges, this asymmetry can still be achieved by employing a result owing to Jones [32], and also adopted by Lamar [37]. Namely, that there is no chordwise loading aft of the maximum span location; Jones gives more details on the correctness of this assumption. The maximum span in the case of side-slipping rectangular wings is drawn schematically in figure 7*a* and shows that the upstream TV always maintains a force along the whole chord length, whereas the effective length of the downstream TV is

$$\frac{x_1}{c} = \begin{cases} 1 - \mathcal{R}\tan\beta & \beta < \beta_1 \\ 0 & \beta \geq \beta_1 \end{cases} \tag{4.20}$$

When x_1 reaches the leading edge at a side-slip angle of $\tan\beta_1 = \mathcal{R}^{-1}$, the downstream TV no longer contributes any force. Finally, we obtain the side-edge vortex coefficient $K_{v,se}$ as

$$K_{v,se} = \frac{1}{\mathcal{R}}\frac{\Gamma_{se}}{Uc}\left[1 + \frac{x_1^2}{c^2}\right] \tag{4.21}$$

Note that as $\mathcal{R} \to \infty$ the condition that the downstream TV does not contribute a force is reached for any $\beta \neq 0$ and thus $K_{v,se} \to 0$ consistent with two-dimensional flow.

(f) Limiting values

So far, the model has represented the flow structure generated by the wing with line vortex segments with prescribed circulation distributions. However, nothing has yet been said about the parameters that characterize the relative circulation magnitudes of these distributions, namely Γ_o, Γ_w, and Γ_{se}. In this section, we apply the results of other well-established wing models in the limiting cases of $\alpha \to 0$ and $\mathcal{R} \to 0$ to obtain estimates for these quantities. We begin with the low-incidence limit and from equation (4.17) $K_p \equiv \lim_{\alpha\to 0} C_{L,\alpha}$ so that K_p is consistent with the lift-curve slope, $C_{L,\alpha}$, at zero angle of attack. We adopt the relation for $C_{L,\alpha}$ first derived by

Helmbold [33], which is known to be accurate for low-$\mathcal{AR}$ unswept or straight wings:

$$K_{\mathrm{p}} = \frac{2\pi\,\mathcal{AR}}{\sqrt{\mathcal{AR}^2+4}+2}. \tag{4.22}$$

From equation (4.18), we can now obtain a relation for Γ_o in terms of K_{p}. As an aside, if one linearizes the Prandtl lifting line ($C_L = 2\pi\,\mathcal{AR}\alpha/(2+\mathcal{AR})$) with respect to $\mathcal{AR}$ it is found that $C_L = \pi\,\mathcal{AR}\alpha$. As a result one will find that, while this does not accurately capture the lift-curve *slope* at zero angle of attack, it does better predict the lift coefficient for a larger angle of attack range for rectangular wings than does Jones' results (figure 6*b*).

Now, moving on to the zero-aspect-ratio limit, we note that K_{p}, $K_{\mathrm{v,le}} \to 0$ and the only remaining term is the side-edge vortex force term. First, we define $\Gamma_{\mathrm{se}} \equiv k_{\mathrm{se}}\Gamma_o$ and use the limiting value of $K_{\mathrm{v,se}}$ to obtain k_{se}. This is done by matching the force coefficient to a slender body model consistent with the prescribed loading, which recalling from §4a it was shown that $K_{\mathrm{v,se}} \to \pi$. Therefore,

$$\lim_{\mathcal{AR}\to 0} K_{\mathrm{v,se}} = \lim_{\mathcal{AR}\to 0}\left(\frac{\partial C_N}{\partial \sin^2\alpha}\right) = k_{\mathrm{se}}\frac{3}{2}\frac{b}{b_{\mathrm{eff}}} = \pi \;\;\rightarrow\;\; k_{\mathrm{se}} = \frac{2\pi}{3}\frac{b_{\mathrm{eff}}}{b} \tag{4.23}$$

Lastly, we need to estimate the wake vortex circulation Γ_{w}. For low-$\mathcal{AR}$ wings, the amount of trailing-edge vorticity that is shed is significantly decreased by the tip vortex downwash assisting in establishing a Kutta condition at the trailing edge [44]. Furthermore, any vorticity that is shed is very quickly wound-up around the tip vortices. Hence, $\Gamma_{\mathrm{te}} \ll \Gamma_{\mathrm{se}} \approx \Gamma_{\mathrm{w}}$. Therefore, we take $\Gamma_{\mathrm{w}} = \Gamma_{\mathrm{se}} = k_{\mathrm{se}}\Gamma_o$. Lastly, the main equations used in the model are collected in appendix A for the reader's convenience.

(g) Roll moment

To compute the roll moment, we must specify where the forces act. The side-edge vortices were assumed to remain attached to their respective tip edge, and so the lateral moment arm is simply the semi-span of the wing, namely $b/2$. Also, because their circulation Γ_x has a linear growth with the chord length, the longitudinal moment arm is $2c/3$ for the upstream TV and $2x_1/3$ for the downstream TV in side-slip. The actual point of action for the resultant of the cross-stream vorticity is slightly more complicated. We first begin by investigating the pitching moment at zero side-slip and then extend the result to non-zero side-slip.

In §4c, the chordwise loading was assumed to be a combination of the constant and 'flat-plate' loading types. As such, the integrated effect is a resultant force that acts somewhere between the quarter-chord and mid-chord points, say x_o. With zero side-slip, there is no roll moment, but there is a pitching moment caused by the vortex structures. For simplicity, we take the point of action to be constant, but note that the overall resultant location is weighted at the wing tips by the side-edge vortex forces acting at $2c/3$ from the leading edge. For planar, unswept wings at low incidence, it is well-known that the moment about the quarter-chord point is nearly zero. Expanding the expression for the pitching moment coefficient, C_{m}, for small α we obtain

$$C_{\mathrm{m}} \approx \left[\left(\frac{1}{4}-\frac{x_o}{c}\right)K_{\mathrm{p}}\right]\alpha + \left[\left(\frac{1}{4}-\frac{x_o}{c}\right)K_{\mathrm{v,le}} - \frac{5}{12}K_{\mathrm{v,se}}\right]\alpha^2. \tag{4.24}$$

To first order in α the potential force, K_{p} obviously acts at the quarter chord. To second order, the vortex forces become appreciable, and x_o will move towards the leading edge to balance the $K_{\mathrm{v,se}}$ moment. At even larger angles of attack, the LESR will increase in size and so will cause x_o to begin to move aft and at this point we can no longer expect that the moment about the quarter chord will be zero. Capturing the complete dependence of x_o on α would introduce undue complexity to the model, perhaps even requiring that the leading-edge potential and vortex forces act in different locations. Therefore, we simply let these forces act at the quarter-chord point and thus the pitching moment about this point is due solely to the side-edge vortices.

Figure 7*b* plots the experimentally measured pitching moment for the $\mathcal{AR} = 1$ wing at $\beta = 0^\circ$ against angle of attack and shows that C_{m} becomes rapidly negative after a certain incidence.

The pitching moment estimated from the model is also plotted and shows qualitative agreement; the slight positive C_m at small angles of attack is not captured and the prediction worsens as α increases. However, we note that these differences are largely dependent on the assumed longitudinal point of action of the side-edge vortices at $2c/3$ from the leading edge, and this does not affect the roll moment which depends on the lateral point of action.

Here, we use the symbol C_l for the rolling moment coefficient; however, it should not be confused with the sectional lift coefficient, which is sometimes given by the same symbol. The rolling moment contribution from the side-edge vortices is simply

$$C_{l,se} = -\frac{K_p}{2\mathcal{R}}\left[1 - \frac{x_1^2}{c^2}\right]\sin^2\alpha, \tag{4.25}$$

where x_1 is given by equation (4.20) and the subtraction between the two terms in the brackets represents the opposing roll moments caused by the upstream and downstream TVs.

For the contribution from the leading-edge forces, we first introduce a coordinate system, x_s–y_s, that is coplanar with the wing and which is rotated by an angle β_s from the body or plate axes, x_p–y_p, such that the x_s-direction is parallel to the freestream flow (figure 7*a*). The angle β_s is related to the actual side-slip angle by $\tan\beta_s = \cos\alpha\tan\beta$. The leading-edge forces create a moment about the y_s axis, which is computed in the x_s–y_s basis, because the expression for the cross-stream circulation γ_y is not relative to the plate coordinates. The component of the resultant moment in the x_p-direction then represents the rolling moment.

The resultant moment is obtained by integrating $x_o(y_s)\gamma_{y_s}$ across the effective span, where $x_o(y_s)$ is the equation of the quarter-chord line relative to the x_s–y_s axes. This line is given by $x_o = \tan\beta_s y_s + x_{o,s}$ where $x_{o,s} = (c/4)\cos\beta_s(1 + \tan^2\beta_s)$. The result yields

$$C_{l,p} = -\frac{1}{\mathcal{R}}\frac{x_{o,s}}{c}[K_p\sin\alpha\cos\alpha]\sin\beta_s \quad \text{and} \quad C_{l,v} = -\frac{1}{\mathcal{R}}\frac{x_{o,s}}{c}[K_{v,le}\sin^2\alpha]\sin\beta_s. \tag{4.26}$$

The total rolling moment coefficient is then $C_l = C_{l,p} + C_{l,v} + C_{l,se}$. These equations are also collected in appendix A.

5. Model comparison and discussion

In this section, the lift, drag and rolling moment are compared with direct force/moment transducer measurements [45]. Discussions on the various contributions to the loads, the effect of aspect ratio and roll stall are also given. The roll moment data displayed a shift in the zero crossing caused by the mounting strategy of the wings. Further testing showed this to be a repeatable, known bias which was removed to align the zero crossing.

Figure 8 plots the lift and drag coefficients as a function of α for the $\beta = 0$ cases. Also shown are the lifting line estimates with the Helmbold equation approximating the lift-curve slope as $\alpha \to 0$ (equation (4.22)). There is a rather good agreement between the model and experiment, with the former accurately capturing the vortex lift associated with the tip vortices and the reattached leading-edge shear layer flow, which cause the lift to depart from the lifting line theory around $\alpha = 10^\circ$, and which is commonly observed for wings with reattached flow. The drag coefficient begins to significantly depart from the induced-drag estimate of lifting line theory at lower angles of attack than does the lift coefficient, and the model shows good agreement up until massive separation and lift stall occurs. For the lift, the vortex contribution quickly subsides with increasing aspect ratio and the lift, not surprisingly, approaches the lifting line estimate. Higher aspect ratios cannot benefit from increased lift from vortex suction, because the flow is unable to reattach. Because the model relies on the assumption of reattached flow, it is not expected to capture the behaviour of the aerodynamic loads beyond the massive separation event.

To show the relative contributions of the forces for a low-$\mathcal{R}$ wing, figure 9*a* plots the different constituents for C_L of the $\mathcal{R} = 1$ wing. It is seen that each force type provides a comparable contribution to the total at moderate angles of attack and that the side-edge vortex force becomes

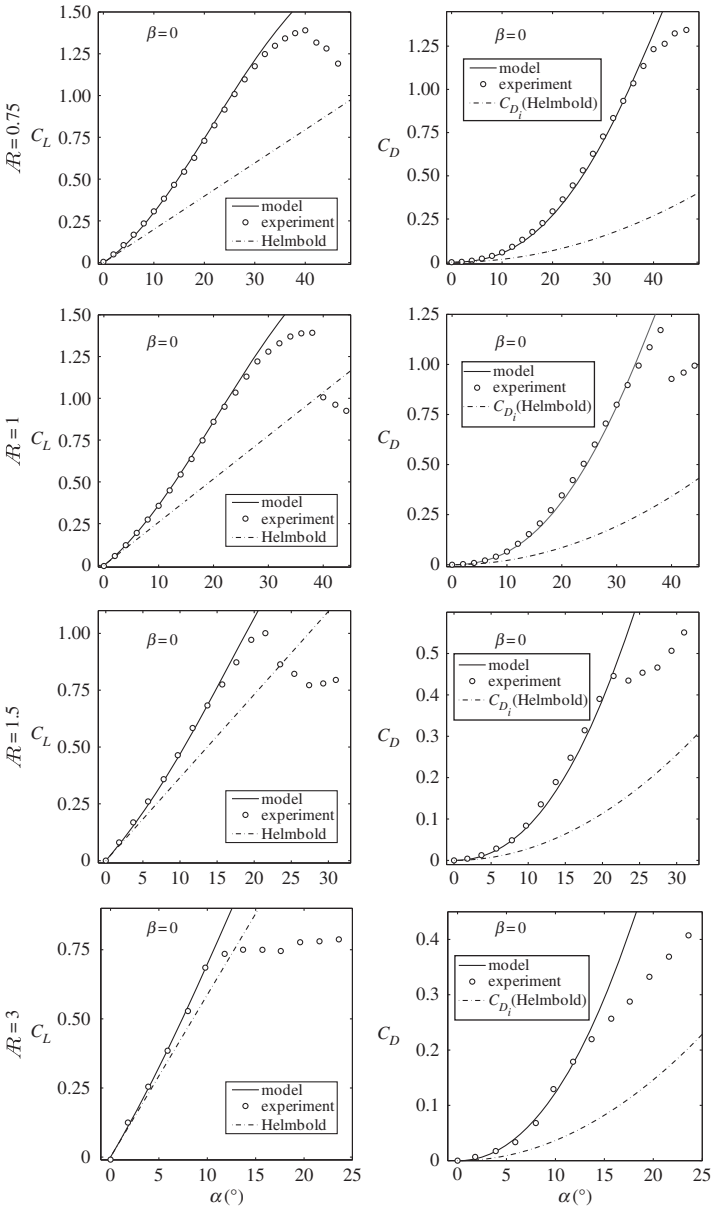

Figure 8. Comparison of force coefficients from the model with experimental measurement for $\beta = 0^\circ$. Also shown are lifting line theory estimates with the Helmbold equation [33]. The left/right columns correspond to the lift/drag coefficients, respectively. The rows from top-to-bottom correspond to aspect ratios $\mathcal{R} = 0.75, 1, 1.5$ and 3.

more significant and begins to dominate as α increases. At high angles of attack, but prior to lift stall, the measured lift decreases slightly from the model curve. The reason for this is that the reattached flow becomes increasingly more intermittent, and during stages of detachment strong trailing-edge vorticity is shed and is not necessarily rolled up into the tip vortices. As such, the total effective circulation Γ_0 is actually lower [44] than predicted by the model, which assumes Γ_0 to be independent of angle of attack. Lastly, figure 9*b* shows a comparison of C_L for the case of $\beta = 10^\circ$ side-slip and for $\mathcal{R} = 0.75$ and 3. There is not much change in the experimentally measured forces from zero side-slip. The model slightly under-predicts the measured forces, but maintains good qualitative agreement.

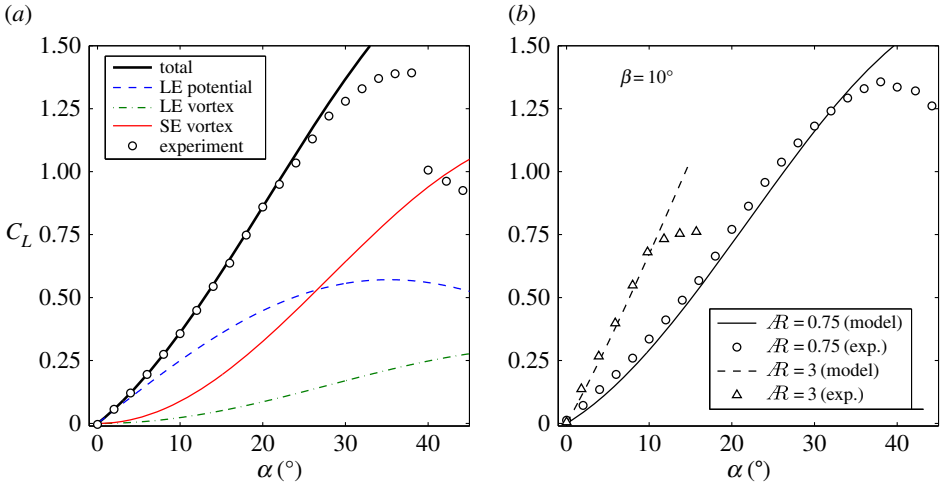

Figure 9. (*a*) Relative contributions to the total lift coefficient for the $\mathcal{R} = 1$ wing at zero side-slip. The contributions include the potential and vortex forces associated with the leading edge and the side-edge vortex force. (*b*) Comparison of the model and experiment for $\beta = 10^\circ$ and $\mathcal{R} = 0.75$ and 3. Data points shortly after lift stall are omitted for clarity. (Online version in colour.)

Next, the roll moment coefficient is considered, and is plotted against side-slip angle β in figure 10 for several different angles of attack; note that the negative of C_l is plotted. For each $\mathcal{R}$ the three lower angles of attack shown occur before roll stall; the highest α corresponds to very near or just after roll stall. Aside from $\mathcal{R} = 3$, which we consider as 'large', the model makes an adequate prediction of the rolling moment for moderate side-slip angles ($\beta < 10^\circ$). However, this depends on whether the flow is reattached, so that for aspect ratios larger than unity the range of applicability is limited to small angles of attack. For low aspect ratios ($\mathcal{R} \leq 1$), the model fares better in its predictions, because the flow remains reattached up to $\alpha = 35$–40°. Despite this, though, the roll moment from the model shows a diverging increase above experiment for $\beta > 20^\circ$ which is significantly exacerbated with increased angle of attack. The experimental data show a slower rate of increase of C_l with increasing β. This implies that at least one of the roll-moment-generating mechanisms does not maintain its effectiveness as the side-slip angle is increased. Levin & Katz [46] showed a similar decrease or drop in the rate of increase of C_l with β for slender delta wings. However, this is attributed to vortex burst occurring over the wing and the aforementioned decrease is much more dramatic than that observed in the current experiments on rectangular wings. This will be discussed further shortly, as a similar decrease in effectiveness is observed with increasing angle of attack and is related to roll stall.

Recall that the roll stall event is similar to lift stall, whereby a near-linear increase with angle of attack of the rolling moment suddenly ceases and C_l begins to decrease in magnitude. Levin & Katz [7] show a very similar behaviour for slender delta wings, and the roll stall event occurs *simultaneously* with lift or normal force stall. This happens, because the vortex lift of slender delta wings is due only to the *two* vortices generated along the highly swept leading edges. However, rectangular low-$\mathcal{R}$ wings are different in that there are *three* main wing edges and corresponding vortices which interact to generate loads on the wing. The different physics involved leads to, for example, roll stall occurring well before lift stall (figure 11*a*). In other words, the disruption of one of the roll-moment-generating mechanisms for the rectangular wing such that the roll moment suddenly decreases does not necessarily affect the lift-generating mechanism of reattachment, as it does for slender delta wings.

Interestingly, for the $\mathcal{R}$ range studied here, both the lift stall and roll stall angles show only about a 1°–2° variation as the side-slip angle β is ranged up to 20° [45]. Figure 11*a* plots the

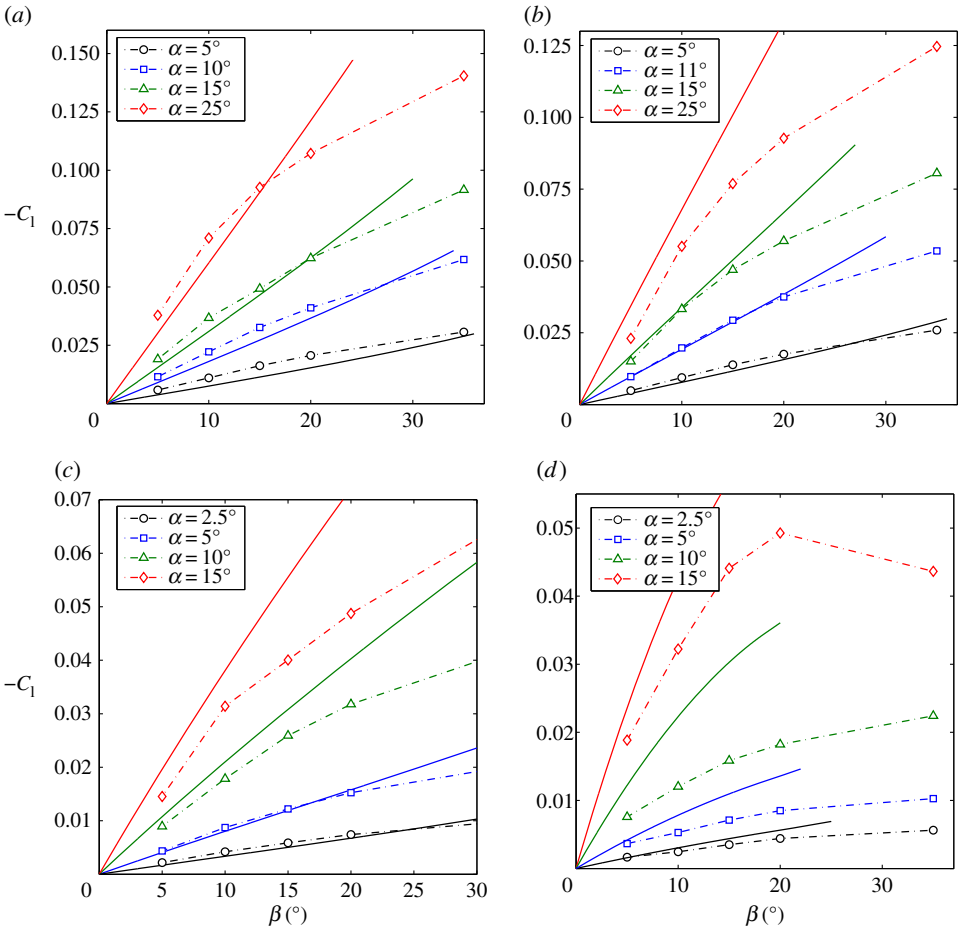

Figure 10. Minus the rolling moment coefficient, $-C_l$, plotted against side-slip angle, β, at several angles of attack for (*a*) $\mathcal{AR} = 0.75$, (*b*) 1, (*c*) 1.5 and (*d*) 3. Symbols are the experimental data, and the solid lines are the model. (Online version in colour.)

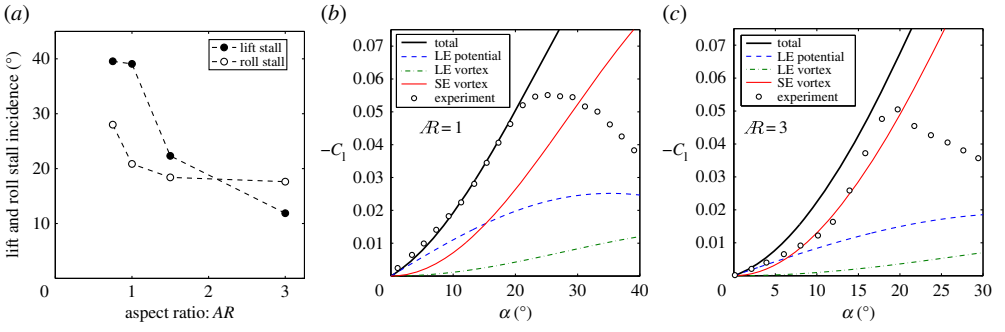

Figure 11. (*a*) The incidence angle at which lift and roll stall occurs as a function of aspect ratio. There is little variation of these angles with side-slip. The rolling moment coefficient $-C_l$ versus α for the (*b*) $\mathcal{AR} = 1$ and (*c*) $\mathcal{AR} = 3$ wings at $\beta = 10°$. Also plotted are the different contributions to the total rolling moment. (Online version in colour.)

average (w.r.t. β) lift and roll stall angles as a function of aspect ratio. Both stall angles decrease as the aspect ratio increases. What is more interesting is that while for $\mathcal{AR} \leq 1$ the roll stall occurs well below the lift stall, there is a dramatic drop in the lift stall angle by $\mathcal{AR} = 1.5$ and roll stall actually occurs after lift stall by $\mathcal{AR} = 3$.

Figure 11*b*,*c* plots the rolling moment coefficient C_l as a function of angle of attack for the $\mathcal{AR} = 1$ and 3 wings both at $\beta = 10^\circ$ side-slip; again note that the negative of C_l is plotted. Also shown are the model predictions and the different contributions to the total rolling moment. For $\mathcal{AR} = 3$, the model over-predicts the measured C_l, but note that after lift stall ($\alpha \approx 12^\circ$) the data better align with the roll moment contribution from just the side-edge vortex (figure 11*c*). This makes sense, because at this angle of attack the leading-edge shear layer is no longer reattached and therefore should not be expected to create potential nor vortex lift (in the sense of the Polhamus method). The upstream side-edge vortex then generates a large moment. However, because the wing is in side-slip, the massive separation spreads across the wing towards the upstream wing edge as α is increased further. When this separation reaches the upstream edge or sufficiently disrupts the side-edge vortex there, then roll stall occurs. This is the most likely explanation of roll stall for *large-aspect-ratio wings*; however, the mechanism is different for low aspect ratios.

For $\mathcal{AR} = 1$, the model predicts the rolling moment quite well prior to roll stall (figure 11*b*) and it is clear that the growth trend is dominated by the side-edge vortex moment. However, the model obviously does not capture the roll stall occurring at $\alpha \approx 21^\circ$. As such, it seems that the roll-moment-generating mechanism that should lose effectiveness is the side-edge vortex. However, we do not believe that this loss of effectiveness is due to vortex breakdown or bursting. The reason is because these low-$\mathcal{AR}$ wings maintain reattached flow, and thus lift generation, up to high angles of attack, whereas vortex breakdown typically results in a detriment to the lift [47]. Moreover, figure 2 shows fairly coherent (time-averaged) vortex structures.

Noting that roll stall is an abrupt change in rolling moment slope, we lastly considered that roll stall is caused by either a *sudden* inboard movement of the upstream TV from its respective side edge and/or a return towards lateral flow symmetry. In the case of the latter, it is possible that the downstream TV may regain some of its roll-moment-generating effectiveness to counteract that of the upstream TV. This seems plausible, because the vortex structures grow in strength with angle of attack. Moreover, this might explain why the behaviour of the decrease in C_l after roll stall is similar to the way it increases from low angles of attack (recall figure 11*b*). Another factor is that locally separated flow may reattach owing to an increased downwash of the side-edge vortices with angle of attack. However, more work is necessary to determine the exact mechanism of roll stall for low-$\mathcal{AR}$ wings.

6. Concluding remarks

The mean flow field around a low-$\mathcal{AR}$ rectangular wing at $\alpha = 35^\circ$ and $Re = 80\,000$ for different side-slip angles of $\beta = 0^\circ$, 10°, 20°, 35° was measured with S-DPIV. The side-slip condition was studied as it has major implications on the lateral loads and dynamics of low-$\mathcal{AR}$ fliers. The objective was to obtain information on the local flow, particularly the vortex structure. The experimental observations were then used to validate high-angle of attack assumptions made in a very simplified model for the aerodynamic loads on the wings.

The development of the model begins with a new interpretation of slender body theory in the limit as the span of a rectangular wing approaches zero and such that its side-edge vortices merge into a vortex doublet or dipole with variable strength in the streamwise direction. From this, we theoretically derived a parabolic spanwise loading, instead of the elliptic distribution associated with fully attached flow in classical aerodynamics. The experimental measurements of the spanwise circulation distribution very closely displayed this parabolic behaviour. The physical explanation is that there is an additional circulation around the wing associated with the reattached flow that comprises the leading-edge separation region. This is a fundamental feature of wings with a broad-facing leading edge and represents a differentiation from delta wings as well as rectangular wings at small incidence. Additionally, the potential solution provides an expression for the dynamic pressure associated with the downwash of the tip vortices that acts to reattach the leading-edge shear layer.

Another interpretation of the slender body potential flow model is to consider it as the zero-aspect-ratio limit of a horseshoe vortex, which is perhaps the simplest representation of a wing. In

the $\mathcal{AR} \to \infty$ limit, the spanwise portion of the vortex system is most important, and as such, the velocity field is dominated by a spanwise monopole distribution of vorticity, and this corresponds to the bound circulation of classical aerodynamics. When $\mathcal{AR} \to 0$, the velocity field is dominated by a streamwise vortex dipole, as we have discussed in this paper. Hence, the spatial range of influence of the flow changes from r^{-1} to r^{-2} as $\mathcal{AR} = \infty$ to 0. One possible ramification of this on the flight of low-$\mathcal{AR}$ vehicles is that conventional control surfaces and their typical location on wings may render them ineffective because they are outside the range where they can affect a change on the dominating vortical structures.

The model is continued by representing the vortex structures by simple line vortices with prescribed circulation distributions motivated by the potential flow model and validated by the experimental measurement. The model is completed by assuming the nonlinear relation between forces and the angle of attack as given by Polhamus' leading-edge suction analogy. The limits of zero angle of attack and zero aspect ratio from well-established models are used to determine remaining parameters. As such, analytical expressions for K_p, $K_\mathrm{v,le}$ and $K_\mathrm{v,se}$ are obtained. For the lift and drag, the model shows excellent agreement with measurement for zero side-slip and a slight under-prediction for non-zero side-slip. Good agreement is obtained as long as reattached flow is maintained, which depends on aspect ratio.

The predicted roll moment showed marginal agreement with measurement and in general is acceptable for $\mathcal{AR} \leq 1$ when $\alpha < 20^\circ$ and up to $\beta = 20^\circ$. For aspect ratios above this, the range of validity with angle of attack decreases very quickly, because massively separated flow occurs at lower incidences. For larger aspect ratios ($\mathcal{AR} \approx 3$), the roll stall mechanism is related to an increasing massive separation region that spreads towards the upstream tip edge as α is increased. When this separation disrupts the upstream tip vortex, a sharp roll stall is observed. The roll stall for low-$\mathcal{AR}$ wings is 'softer', similar to trends in the lift stall. However, the model does not explicitly capture roll stall, and it was presumed that roll stall is caused by a return to lateral flow structure symmetry. Very recent work by our co-workers (Linehan & Mohseni) has confirmed this hypothesis and elucidates more details of the roll stall mechanism. Namely, there is a spanwise distribution in the 'amount' of unsteady flow reattachment. Initially, there is an asymmetry in this distribution that causes the induced roll moment. However, as the angle of attack is increased the strength of the tip vortex downwash also increases. At the roll stall incidence, this downwash becomes strong enough to increase the level of reattachment on the downstream wing side. As such, the total lift is still maintained, but the asymmetry in the distribution is reduced and thus the roll moment begins to decrease, thus causing roll stall. Future work is required to determine how this could be incorporated into the current model.

Data accessibility. The relevant data associated with this work are found in the paper.

Authors' contributions. A.C.D. performed the experiments and data analysis. A.C.D. developed the mathematical model through several valuable discussions with K.M.

Competing interests. We have no competing interests.

Funding. This work was supported by the Air Force Office of Scientific Research.

Acknowledgements. The authors thank the anonymous reviewers, whose comments strengthened the overall manuscript. We also would like to thank Thomas Linehan for providing the force and moment transducer measurements presented in this paper.

Appendix A: model summary

Here, the main expressions of the model developed in §4 are collected. The expressions for Γ_o, Γ_se, Γ_w and k_se have all been written in terms of K_p to give

force coefficients	rolling moment coefficient
$C_L = C_N \cos\alpha$	$C_\mathrm{l} = C_\mathrm{l,p} + C_\mathrm{l,v} + C_\mathrm{l,se}$
$C_D = C_N \sin\alpha$	$C_\mathrm{l,p} = -\dfrac{1}{\mathcal{AR}} \dfrac{x_{o,s}}{c} [K_\mathrm{p} \sin\alpha \cos\alpha] \sin\beta_\mathrm{s}$

$$C_N = K_p \sin\alpha\cos\alpha + K_v \sin^2\alpha$$

$$K_p = \frac{2\pi \mathcal{R}}{\sqrt{\mathcal{R}^2+4}+2}$$

$$K_v = K_{v,le} + K_{v,se}$$

$$K_{v,le} = K_p(1 - K_i K_p)$$

$$K_{v,se} = \frac{K_p}{\mathcal{R}}\left[1 + \frac{x_1^2}{c^2}\right]$$

$$K_i = \frac{1}{\pi \mathcal{R}}\frac{b}{b_{eff}}$$

$$\frac{x_1}{c} = 1 - \mathcal{R}\tan\beta, \quad \frac{b_{eff}}{b} = \cos\beta + \frac{\sin\beta}{\mathcal{R}}.$$

$$C_{l,v} = -\frac{1}{\mathcal{R}}\frac{x_{o,s}}{c}[K_{v,le}\sin^2\alpha]\sin\beta_s$$

$$C_{l,se} = -\frac{K_p}{2\mathcal{R}}\left[1 - \frac{x_1^2}{c^2}\right]\sin^2\alpha$$

$$\frac{x_{o,s}}{c} = \frac{1}{4}\cos\beta_s(1+\tan^2\beta_s)$$

$$\tan\beta_s = \cos\alpha\tan\beta.$$

The quantity, $K_p K_i = (2/3\mathcal{R})(\Gamma_o/Uc)$, can be considered as a constant, effective downwash on the vortex system as in Polhamus [16]. Comparing with the Prandtl lifting line result of $(1/2\mathcal{R})(\Gamma_o/Uc)$, the downwash associated with reattached flow is 33% stronger for a given aspect ratio, and the induced drag $C_{D,i} = K_i C_L^2$ is the same, but the total vortex drag rapidly mounts with increasing angle of attack.

References

1. Taira K, Colonius T. 2009 Three-dimensional flows around low-aspect-ratio flat-plate wings at low Reynolds numbers. *J. Fluid Mech.* **623**, 187–207. (doi:10.1017/S0022112008005314)
2. Pisano WJ, Lawrence DA. 2007 Autonomous UAV control using a 3-sensor autopilot. In *Proc. AIAA Aerospace Sciences Meeting, number 2007-2756, Rohnert Park, CA, 7–10 May*. Reston, VA: AIAA.
3. Shaw A, Mohseni K. 2011 A fluid dynamic based coordination of a wireless sensor network of unmanned aerial vehicles: 3-D simulation and wireless communication characterization. *IEEE Sensors J. Special Issue Cogn. Sensor Netw.* **11**, 722–736. (doi:10.1109/JSEN.2010.2064294)
4. Shields M, Mohseni K. 2015 Inherent stability modes of low aspect ratio wings. *J. Aircraft* **52**, 141–155. (doi:10.2514/1.C032636)
5. Grasmeyer JM, Keennon MT. 2001 Development of the Black Widow micro air vehicle. In *Proc. the AIAA Aerospace Sciences Meeting and Exhibit, number 2001-0127, Reno, NV, 8–11 January*. Reston, VA: AIAA.
6. Watkins S, Milbank J, Loxton BJ, Melbourne WH. 2006 Atmospheric winds and their implications for micro air vehicles. *AIAA J.* **44**, 2591–2600. (doi:10.2514/1.22670)
7. Levin D, Katz J. 1984 Dynamic load measurements with delta wings undergoing self-induced roll oscillations. *J. Aircraft* **21**, 30–36. (doi:10.2514/3.48218)
8. Ericsson LE. 1995 Wing rock analysis of slender delta wings, review and extension. *J. Aircraft* **32**, 1221–1226. (doi:10.2514/3.46867)
9. Gresham NT, Wang Z, Gursul I. 2010 Low Reynolds number aerodynamics of free-to-roll low aspect ratio wings. *Exp. Fluids* **49**, 11–25. (doi:10.1007/s00348-009-0726-2)
10. Pullin DI. 1972 Calculations of the steady conical flow past a yawed slender Delta wing with leading-edge separation. Technical Report R&M 3767. London, UK: Aeronautical Research Council, Imperial College of Science and Technology.
11. Verhaagen NG, Naarding HJ. 1989 Experimental and numerical investigation of vortex flow over a sideslipping Delta wing. *J. Aircraft* **26**, 971–978. (doi:10.2514/3.45869)
12. Verhaagen NG, Jobe CE. 2003 Wind tunnel study of a 65-deg Delta wing at sideslip. *J. Aircraft* **40**, 290–296. (doi:10.2514/2.3092)
13. Shields M, Mohseni K. 2012 Effects of sideslip on the aerodynamics of low aspect ratio wings at low Reynolds numbers. *AIAA J.* **50**, 85–99. (doi:10.2514/1.J051151)
14. Shields M, Mohseni K. 2013 Roll stall for low-aspect-ratio wings. *J. Aircraft* **50**, 1060–1069. (doi:10.2514/1.C031933)

15. Shields M, Mohseni K. 2013 Passive mitigation of roll stall for low aspect ratio wings. *Adv. Robot.* **27**, 667–681. (doi:10.1080/01691864.2013.778941)
16. Polhamus EC. 1966 A concept of the vortex lift of sharp-edge delta wings based on a leading-edge suction analogy. Technical Report TN D-3767. Hampton, VA: NASA, Langley Research Center.
17. Soloff SM, Adrian RJ, Liu ZC. 1997 Distortion compensation for generalized stereoscopic particle image velocimetry. *Meas. Sci. Technol.* **8**, 1441–1454. (doi:10.1088/0957-0233/8/12/008)
18. Willert C. 1997 Stereoscopic digital particle image velocimetry for application in wind tunnel flows. *Meas. Sci. Technol.* **8**, 1465–1479. (doi:10.1088/0957-0233/8/12/010)
19. Wieneke B. 2005 Stereo-PIV using self-calibration on particle images. *Exp. Fluids* **39**, 267–280. (doi:10.1007/s00348-005-0962-z)
20. Westerweel J. 2000 Theoretical analysis of the measurement precision in particle image velocimetry. *Exp. Fluids* **29**, S3–S12. (doi:10.1007/s003480070002)
21. Raffel M, Willert CE, Kompenhans J. 1998 *Particle image velocimetry*. New York City, NY: Springer.
22. Yilmaz TO, Rockwell D. 2010 Three-dimensional flow structure on a maneuvering wing. *Exp. Fluids* **48**, 539–544. (doi:10.1007/s00348-009-0772-9)
23. Visbal. MR. 2011 Three-dimensional flow structure on a headving low-aspect-ratio wing. In *Proc. 49th AIAA Aerospace Sciences Meeting*, *number 2011-219, Orlando, FL, 4–7 January*, pp. 1–24. Reston, VA: AIAA.
24. Jian T, Ke-Qin Z. 2004 Numerical and experimental study of flow structure of low-aspect-ratio wings. *J. Aircraft* **41**, 1196–1201. (doi:10.2514/1.5467)
25. Wu JZ, Wu JM, Wu CJ. 1987 A general three-dimensional viscous compressible theory on the interaction of solid body and vorticity-dilatation field. Technical Report UTSI Report 87/03. Tullahoma, TN: University of Tennessee Space Institute.
26. Perry AE, Chong MS. 1994 Topology of flow patterns in vortex motions and turbulence. *Appl. Sci. Res.* **53**, 357–374. (doi:10.1007/BF00849110)
27. DeVoria AC, Ringuette MJ. 2012 Vortex formation and saturation for low-aspect-ratio rotating flat-plate fins. *Exp. Fluids* **52**, 441–462. (doi:10.1007/s00348-011-1230-z)
28. Gursul I, Gordnier R, Visbal M. 2005 Unsteady aerodynamics of nonslender delta wings. *Prog. Aerosp. Sci.* **41**, 515–557. (doi:10.1016/j.paerosci.2005.09.002)
29. Prandtl L. 1921 Applications of modern hydrodynamics to aeronautics. Technical report no. 116. National Advisory Committee for Aeronautics.
30. Bollay W. 1939 A nonlinear wing theory and its application to rectangular wings of small aspect ratio. *Z. Agnew. Math. Mech.* **19**, 21–35. (doi:10.1002/zamm.19390190103)
31. Falkner VM. 1943 The calculation of aerodynamic surfaces of any shape. Report ARC R&M 1910. London, UK: Ministry of Technology.
32. Jones RT. 1946 Properties of low-aspect-ratio pointed wings at speeds below and above the speed of sound. *J. Eng. Math.* **19**, 157–172.
33. Helmbold HB. 1942 Der unvurwundene ellipsenfliigel als tragende fliiche. Report, der Deutschen Luftfahrt-forschung, R. Oldenbourg (Munich).
34. Küchemann D. 1956 Der unvurwundene ellipsenfliigel als tragende fliiche. Report no. 2935, Ministry of Supply.
35. Brown CE, Michael WH. 1954 Effect of leading-edge separation on the lift of a delta wing. *J. Aeronaut. Sci.* **21**, 690–694. (doi:10.2514/8.3180)
36. Mangler KW, Smith JHB. 1959 A theory of the flow past a slender delta wing with leading edge separation. *Proc. R. Soc. Lond. A* **251**, 200–217. (doi:10.1098/rspa.1959.0102)
37. Lamar JE. 1974 Extension of leading-edge suction analogy to wings with separated flow around the side edges at subsonic speeds. Technical Report TR R-428. Hampton, VA: NASA, Langley Research Center.
38. Multhopp H. 1950 Methods for calculating the lift distribution of wings (subsonic lifting-surface theory). Report no. 29884, Ministry of Supply.
39. Riley N, Smith JHB. 1985 Prediction of leading-edge behavior to supplement the suction analogy. *J. Eng. Math.* **19**, 157–172. (doi:10.1007/BF00042738)
40. Clark RW, Smith JHB, Thompson CW. 1975 Some series expansion solutions for slender wings with leading-edge separation. Report ARC R&M 3785. London, UK: Ministry of Defence.
41. Cole JD. 1968 *Perturbation methods in applied mathematics*, 1st edn. Waltham, MA: Blaisdell Publishing Company.

42. Hemsch MJ, Luckring JM. 1990 Connection between leading-edge sweep, vortex lift, and vortex strength for delta wings. *J. Aircraft* **27**, 473–475. (doi:10.2514/3.25305)
43. Milne-Thomson LM. 1958 *Theoretical aerodynamics*. Mineola, NY: Dover.
44. DeVoria AC, Mohseni K. 2017 On the mechanism of high-incidence lift generation for steadily translating low-aspect-ratio wings. *J. Fluid Mech.* **813**, 110–126. (doi:10.1017/jfm.2016.849)
45. Linehan T, Mohseni K. 2016 Aerodynamics and lateral stability of low-aspect-ratio wings with dihedral at low Reynolds numbers. In *Proc. AIAA Aerospace Sciences Meeting*, *number 2016-1063, San Diego, CA, 4–8 January*. Reston, VA: AIAA.
46. Katz J, Levin D. 1991 Static measurements of slender delta wing rolling moment hysteresis. *J. Aircraft* **28**, 282–283. (doi:10.2514/3.46024)
47. Gursul I. 2005 Review of unsteady vortex flows over slender delta wings. *J. Aircraft* **42**, 299–319. (doi:10.2514/1.5269)